Nano Research 2018, 11(4): 1883–1894
https://doi.org/10.1007/s12274-017-1806-x
Research Article
ISSN 1998-0124
CN 11-5974/O4

Fast formation of single-unit-cell-thick and defect-rich layered double hydroxide nanosheets with highly enhanced oxygen evolution reaction for water splitting

Rui Gao[1] and Dongpeng Yan[1,2] (✉)

[1] *State Key Laboratory of Chemical Resource Engineering, Beijing University of Chemical Technology, Beijing 100029, China*
[2] *Beijing Key Laboratory of Energy Conversion and Storage Materials, College of Chemistry, Beijing Normal University, Beijing 100875, China*

Received: 18 July 2017
Revised: 8 August 2017
Accepted: 15 August 2017

KEYWORDS
single-unit-cell,
defect-rich,
oxygen evolution reaction,
water splitting

ABSTRACT

The development of high-efficiency electrocatalysts for oxygen evolution reactions (OERs) plays an important role in the water-splitting process. Herein, we report a facile way to obtain two-dimensional (2D) single-unit-cell-thick layered double hydroxide (LDH) nanosheets (NSs, ~ 1.3 nm) within only 5 min. These nanosheets presented significantly enhanced OER performance compared to bulk LDH systems fabricated using the conventional co-precipitation method. The current strategy further allowed control over the chemical compositions and electrochemical activities of the LDH NSs. For example, CoFe-LDH NSs presented the lowest overpotential of 0.28 V at 10 mA/cm^2, and the NiFe-LDHs NSs showed Tafel slopes of 33.4 mV/decade and nearly 100% faradaic efficiency, thus outperforming state-of-the-art IrO_2 water electrolysis catalysts. Moreover, positron annihilation lifetime spectroscopy and high-resolution transmission electron microscopy observations confirmed that rich defects and distorted lattices occurred within the 2D LDH NSs, which could supply abundant electrochemically active OER sites. Periodic calculations based on density functional theory (DFT) further showed that the CoFe- and NiFe-LDHs presented very low energy gaps and obvious spin-polarization behavior, which facilitated high electron mobility during the OER process. Therefore, this work presents a combined experimental and theoretical study on 2D single-unit-cell-thick LDH NSs with high OER activities, which have potential application in water splitting for renewable energy.

1 Introduction

With the rapid growth of the power industry in the world, a new energy era has quietly arrived because of the influences of the energy crisis, environmental protection, and low carbon economy [1–3]. The oxygen

Address correspondence to yandp@mail.buct.edu.cn, yandp@bnu.edu.cn

evolution reaction (OER) is particularly critical for clean and renewable energy technologies, such as fuel cells, batteries, and water-splitting processes [4–8]. Usually, the OER process imposes a high overpotential requirement, and hence it seriously hinders large-scale hydrogen production from water splitting [9–12]. State-of-the-art precious metal catalysts (e.g., IrO_2 and RuO_2) could exhibit superior OER activity but they suffer from low abundance and high cost [13–15]. As alternative systems, two-dimensional (2D) micro/nanostructures (such as 2D g-C_3N_4 nanosheets [16] and layered selenides [17]) have become of great interest recently because they exhibit high OER catalytic activity. However, their low number of exposed surface-active sites and relatively complicated synthesis methods (e.g., high-temperature hydrothermal process) have restricted their effective utilization in practical applications [17–20]. Compared with typical 2D-layered catalysts, ultrathin atomically scaled or single-unit-cell-thick nanosheets (NSs) have shown enhanced catalytic performance because of their improved intrinsic catalytic activity and electronic conductivity [19, 21, 22]. For example, 2D single-unit-cell-thick $CoSe_2$ nanosheets presented good OER performance because of the exposure of 66.7% Co^{2+} ions as catalytically active sites on the surface [21]. In addition, the slight structural distortion in atomically thin 2D structures has been demonstrated to enhance water absorption and hence favor OER reaction kinetics [23, 24]. Moreover, the electrocatalytic activity of transition metal-based catalysts is also related to the spin states of the metal atoms, which can be delocalized after introducing structural distortion to the atomic layers [25]. Therefore, developing ideal ultrathin atomic-scaled thick NS catalysts with abundant active sites could serve as a good way to achieve high-efficiency water electrolysis. Furthermore, considering future commercial application, a facile synthesis method with advantages of universal applicability, moderate reaction conditions, low cost, and high production yield is also significant.

Layered double hydroxides (LDHs) are a family of 2D clay compounds containing divalent and trivalent metal cations, which are able to combine electrochemically active elements such as Ni, Fe, Co, and many others [26–30]. For instance, the NiFe-LDH system has been investigated as an efficient OER catalyst owing to its high activity and stability in basic media; various strategies have been developed to further improve its performance either by hybridizing it with carbon materials or by constructing micro/nanostructures [18, 19, 31, 32]. For example, Hu et al. demonstrated that exfoliated LDH NSs showed significantly enhanced performance as compared to their bulk phase due to their improved intrinsic catalytic activity and conductivity [19]. However, the synthesis of exfoliated LDH NSs not only required complicated multi-step procedures (i.e., hydrothermal process, anion exchange, and exfoliation) but also required two or more days at least to achieve the final product [19, 31–34]. Additionally, the production yield was relatively low. It is therefore desirable to employ a simple and alternative way to synthesize different kinds of ultrathin atomic-scaled thick LDH NSs, which could increase the number of active edge sites with higher electronic conductivity.

To achieve this important goal, herein, we report an effective way to obtain ultrathin atomic-thick LDH layers within only 5 min [35]. Representative atomic-thick LDH NSs such as CoNi-, NiFe-, CoFe-, and ZnCo-LDHs were constructed as ideal model systems, which showed much higher OER activities (in terms of overpotential, turnover frequency, double-layer capacitance, and stability) than bulk LDHs using the typical co-precipitation method. For example, the NiFe-LDH NSs exhibited lower overpotential and higher stability than a state-of-the-art IrO_2 catalyst. Owing to the rapid synthesis and ultrathin NSs, the unique 2D nanostructures exhibited more surface defects, which could serve as active sites to achieve efficient catalysis of the OER. Density functional theory (DFT) calculations also provide fundamental insight into the electronic structures of the different LDHs and confirmed the higher electronic conductivity and spin-polarization characteristics for Fe-based LDH NCs. Therefore, this work not only presents a facile strategy to obtain 2D atomic-thick NSs toward highly enhanced OER activity but also supplies a detailed understanding of the electronic structures of LDH nanostructures from a theoretical perspective.

2 Experimental

2.1 Materials

Formamide, $Zn(NO_3)_2·6H_2O$, $Co(NO_3)_2·6H_2O$, $Ni(NO_3)_2·6H_2O$, $Fe(NO_3)_3·9H_2O$, $NaNO_3$, NaOH, and IrO_2 were purchased from Aladdin Chemical Co. Ltd. The chemicals were all of analytical grade and were used without purification. Deionized water was used in all the experimental processes.

2.2 Synthesis of ultrathin atomic-scale-thick LDH nanosheets

Taking CoFe-LDH nanosheets as an example, first, for solution A, $Co(NO_3)_2·6H_2O$ (0.0006 mol) and $Fe(NO_3)_3·9H_2O$ (0.0002 mol) were dissolved in 10 mL of deionized water. For solution B, NaOH (0.005 mol) was dissolved in 10 mL of deionized water. For solution C, $NaNO_3$ (0.0002 mol) was dissolved in a mixed solvent containing 7 mL of deionized water and 3 mL of formamide. Solution A and solution B were added into solution C dropwise with stirring at 80 ˚C to maintain the system at a pH value of ~ 10. After 5 min, the resulting precipitation was centrifuged and washed with deionized water several times. A dialysis (8 kDa) treatment was performed to remove the formamide so as to obtain the final LDH nanosheets. The sediment was diluted to 10 mL using deionized water. Other LDH samples were prepared by the same procedure using their respective starting materials.

2.3 Characterization

Powder X-ray diffraction (XRD) patterns of all the samples were carried out using graphite-filtered Cu Kα radiation operating at 40 kV and 30 mA, λ = 0.15418 nm (Shimadzu XRD-6000 diffractometer). The morphology of the samples was investigated by using a scanning electron microscope (SEM, Hitachi S-3500) equipped with an energy dispersive X-ray (EDX) attachment (Oxford Instruments Isis 300) with an acceleration voltage of 20 kV. High-resolution transmission electron microscope (HRTEM) images were recorded on a JEOL JEM-2100 TEM with an accelerating voltage of 200 kV. Atomic force microscopy (AFM) images were recorded on a NanoScope IIIa from Veeco Instruments. Inductively coupled plasma atomic emission spectroscopy (ICP-AES, Shimadzu ICPS-7500) was used to analyze the metal content of the samples. Photon correlation spectroscopy (PCS) was conducted to record the zeta potential, and the dynamic light-scattering (DLS) diameter was measured on a Nanosizer Nano ZS system from MALVERN Instruments. Positron annihilation measurements were taken with a fast–slow coincidence ORTEC system with a time resolution of 187 ps for the full width at half-maximum.

2.4 Electrode preparation

For IrO_2 and bulk LDH nanoparticles, a homogeneous catalyst ink was obtained by sonicating 1.0 mg of powders in 1.0 mL of water for 30 min. For ultrathin single-unit-cell-thick LDH nanosheets, a homogeneous catalyst ink consisting of 2.0 mL of the dialysis solution and 8 mL of deionized water was obtained by sonication for 30 min. Glassy carbon disk electrodes with diameters of 3 mm were used. The electrodes were polished with two different alpha alumina powders (1.0 and 0.3 mm, from CH Instruments) suspended in deionized water on a nylon polishing pad (CH Instruments) and with gamma alumina powder (0.05 mm from CH Instruments) suspended in distilled water on a micro-cloth polishing pad (CH Instruments). After the first and second stages of cleaning, the electrodes were thoroughly rinsed with deionized water. Before being loaded with catalysts, the electrodes were also cleaned in acetone by sonication for approximately 10 s. The catalysts (10 μL) were then drop-casted on the glassy carbon disk electrode and the solvent was allowed to be evaporated at room temperature.

2.5 Electrochemical tests

All electrochemical measurements were carried out on an electrochemical workstation (CHI 660C, CH Instrument Co. USA). Ag/AgCl and Pt wire were used as the reference and counter electrodes, respectively. Linear sweep voltammetry with a scan rate of 10 mV/s was conducted in 0.1 M KOH. The KOH electrolyte was degassed by bubbling oxygen for 30 min. All the potentials were calibrated to a reversible hydrogen electrode (RHE). Cyclic voltammetry (CV) was performed at various scan rates (1, 5, 10, 50, 100, and 200 mV/s) versus RHE region. The double-layer

capacitance (C_{dl}) was estimated by plotting Δj ($j_a - j_c$) against the scan rates, where j_a and j_c are the anodic and cathodic current densities, respectively. The slope was twice that of the C_{dl}. The faradaic efficiency was calculated by comparing the amount of gas theoretically calculated and experimentally measured. The faradaic yield was calculated from the total amount of charge Q (C) passed through the cell and the total amount of oxygen produced (n_{O2}: mmol). Assuming that four electrons are needed to produce one O_2 molecule, the faradaic efficiency was calculated as faradaic efficiency = $4F \times \frac{n_{O_2}}{Q} = 4F \times n_{O_2} \times 10 / t$, where F is the Faraday constant, $Q = t \times 0.1$ (C), and t is the time (s) for the constant oxidation current. The total amount of oxygen produced was measured using the drainage method. To assess the faradic efficiency, we collected O_2 by the water–gas displacing method and calculated the mole values of O_2 generated from the water splitting. We then calculated the theoretical amount of O_2 with an I–t curve by applying the Faraday law. The apparent turnover frequency (TOF) was calculated from the equation TOC = $j \times A/(4F \times m)$, where j is the current density at a given overpotential, A is the surface area of the electrode, F is the Faraday constant (96,485 C/mol), and m is the mole number of metal on the electrode. This TOF was estimated by assuming that all the electroactive metal atoms in the LDH electrodes were catalytically active for the OER.

2.6 Structural model and DFT calculation

Ideal LDH layers with a 4 × 3 × 1 rhombohedral supercell with an $R3m$ space group containing 12 metal atoms was built according to our previous work [34, 36]. The lattice parameters of the 2D layer were $a = b = 2d_{110} = 3.05$ Å based on experimental results. The supercell of the octahedral layer had 12 metal atoms and 24 OH groups under the condition of $\alpha = \beta = 90°$, and the distance between adjacent metal atoms was 3.05 Å. The ratios of Ni/Fe, Co/Ni, Co/Fe, and Zn/Co were 3:1, which is very close to the experimental results. Therefore, a supercell was constructed with the initial values of $c = 8$ Å (experimental results) and $\alpha = \beta = \gamma = 90°$. The DFT method was performed using the Dmol3 [37] module in the Material Studio software package [38]. The configurations were optimized by the Perdew–Wang (PW91) [39] generalized gradient approximation (GGA) method with double numerical basis sets plus polarization function (DNP). The core electrons for the metals were treated by effective core potentials (ECP). The SCF converged criterion was within 10^{-5} hartree/atom and the converged criterion of the structure optimization was 10^{-3} hartree/bohr. The Brillouin zone was sampled by 1 × 1 × 1 k points, and test calculations revealed that the increase of k points did not influence the results.

3 Results and discussion

The ultrathin LDH NSs were synthesized through a facile and rapid precipitation method with both formamide and water as solvents (Fig. 1(a)). The as-obtained LDH colloids did not show the typical (003) diffraction peak at $2\theta \approx 11.68°$, indicating the lack of long-range ordered stacking in the c-axis direction (Fig. 1(c) and Fig. S1 in the Electronic Supplementary Material (ESM): green lines). When the LDH samples were dried, broad and intensive (003) and (006) diffraction peaks appeared (Fig. 1(c) and Fig. S1 in the ESM: orange lines), which are ascribed to the re-stacking of LDH NSs during solvent evaporation. Figure 1(d) and Fig. S2 (in the ESM) show the representative AFM images of the individual LDH particles with thicknesses of ~ 1.3 nm and widths of 40 nm. The height is very close to the single-unit-cell spacing in the (00l) direction (~ 0.8 nm) for CO^{3-}/LDHs [40]. The thickness values are slightly higher than those of the atomically single-layer LDH NSs (0.8–1 nm) as determined through the liquid exfoliation method [19, 41, 42], probably because of the residual anions and/or solvent molecules at the LDH surfaces. Such observations confirm the successful synthesis of ultrathin single-unit-cell-thick LDH NSs. The compositions of these NSs were measured by ICP-AES (Table S1 in the ESM), which maintains the initial ratio of M^{2+}/M^{3+} LDH NSs. To reveal the microstructures of the ultrathin single-unit-cell-thick LDH NSs, the samples were further characterized by HRTEM, from which uniform hexagonal plates with lateral sizes of ~ 40 nm were observed (Fig. 1(e) and Fig. S3(a) in the ESM). The lattice fringe of 0.159 nm is attributed to the (110)

plane of the LDH phase (Fig. 1(f)). The edges of the NSs were flawed and the lattice had some distortion (insets in Fig. 1(f) and Fig. S3 in the ESM) because the flawed and distorted lattices could decrease the surface/interfacial energy and thus favor the structural stability of the 2D ultrathin NSs during the rapid synthesis process. These microscopic characteristics were conducive to the development of numerous active edge sites because it has been reported that lattice defects have a positive effect on the enhancement of OER electrocatalysis [43]. Moreover, the average hydrodynamic diameter of the LDH NSs in aqueous solution was estimated to be 40–50 nm (Fig. S4 in the ESM), similar to the size observed by HRTEM. The stability of the as-obtained LDH NS dispersion was further studied. Taking NiFe-LDH NSs as an example (Fig. S5 in the ESM), the NiFe-LDH NSs in a colloid presented obvious Tyndall light scattering at 0, 10, 20, and 30 days, suggesting high dispersion of the NiFe-LDH NSs. The particle distribution revealed that the pseudo-hexagonal NSs maintained nearly the same size distribution over 30 days. Hence, the stable time of the NiFe-LDH NS dispersion can last for 30 days at least. The zeta potential measurement (Fig. S6 in the ESM) showed that the surfaces of the ultrathin LDH NSs were positively charged, with values of 25–40 mV at pH 10, which could supply electrostatic repulsion to reduce the aggregation of the LDH NSs. Also, the positive potential would facilitate the surface absorption of OH^-/H_2O in the OER process, based on electrostatic and/or ion-dipolar interactions.

To effectively illustrate the role of ultrathin single-unit-cell-thick LDH NSs on the electrocatalytic performance, we also synthesized 2D bulk LDHs (i.e., CoNi-LDHs, NiFe-LDHs, CoFe-LDHs, and ZnCo-LDHs) by using the typical co-precipitation method. The XRD patterns (Fig. S7 in the ESM) confirmed the pure phase of the LDH particles. The SEM images revealed that the size of the bulk LDHs was approximately 40 nm (Fig. S8 in the ESM), which is similar to the size of the ultrathin single-unit-cell-thick LDH NSs (Fig. 1(e) and Fig. S3(a) in the ESM). However, the thickness of the bulk LDHs was estimated to be more than 10 nm, much higher than the thickness of the NSs. Moreover,

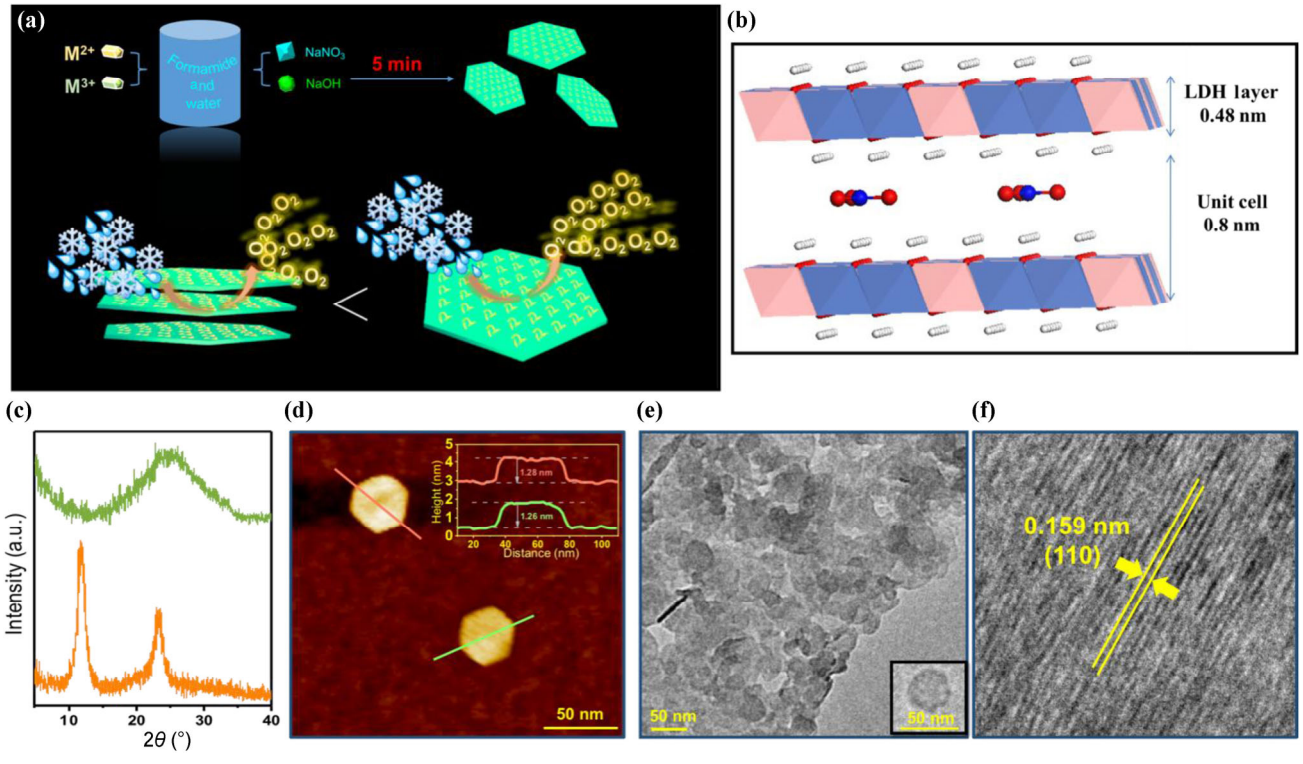

Figure 1 (a) and (b) Schematic illustration for the formation of ultrathin single-unit-cell-thick LDH NSs and their application in OER, (c) XRD patterns of colloid (green line) and the re-stacking of ultrathin single-unit-cell-thick NiFe-LDH NSs (orange line), (d) AFM image and the corresponding height profiles, (e) TEM image, and (f) HRTEM image.

commercial IrO_2 was further chosen as the standard control to compare single-unit-cell-thick LDH NSs. As shown in Fig. S9(a) (in the ESM), the XRD peaks of the powder are consistent with the IrO_2 phase (JCPDS Card No. 43-1019), suggesting the high purity of the resulting samples. The SEM image revealed that the particle size is approximately 20 nm (Fig. S9(b) in the ESM).

The ultrathin single-unit-cell-thick NSs and bulk LDHs were then tested for electrochemical OER in a 0.1 M KOH solution using a standard three-electrode system. Figure 2(a) shows that the linear sweep voltammetry (LSV) curves of LDH NSs with different compositions. It is observed that the overpotentials (η) at a current density of 10 mA/cm^2 of the ultrathin LDH NSs are much lower than those of the corresponding bulk LDHs—the η values decreased by 70, 72, 81, and 49 mV relative to the bulk CoNi-, NiFe-, CoFe-, and ZnCo-LDH systems, respectively (Fig. 2(b)). The current density values at η = 300 mV for the ultrathin CoNi-, NiFe-, CoFe-, and ZnCo-LDH NSs were ~ 7.3, 6.3, 6.7, and 1.6 times larger than those of the bulk LDH electrodes, respectively (Fig. 2(c)). The Tafel slope is usually used to study the catalytic mechanism of electrocatalysis for OER. The dramatic enhancement in catalytic activity of the LDH NSs is also reflected in their lower Tafel slopes (Fig. 2(a) inset). The Tafel slope values of the ultrathin CoNi-, NiFe-, CoFe-, and ZnCo-LDH NSs were 46.1, 33.4, 58.2, and 44.1 mV/decade, whereas those of the bulk CoNi-,

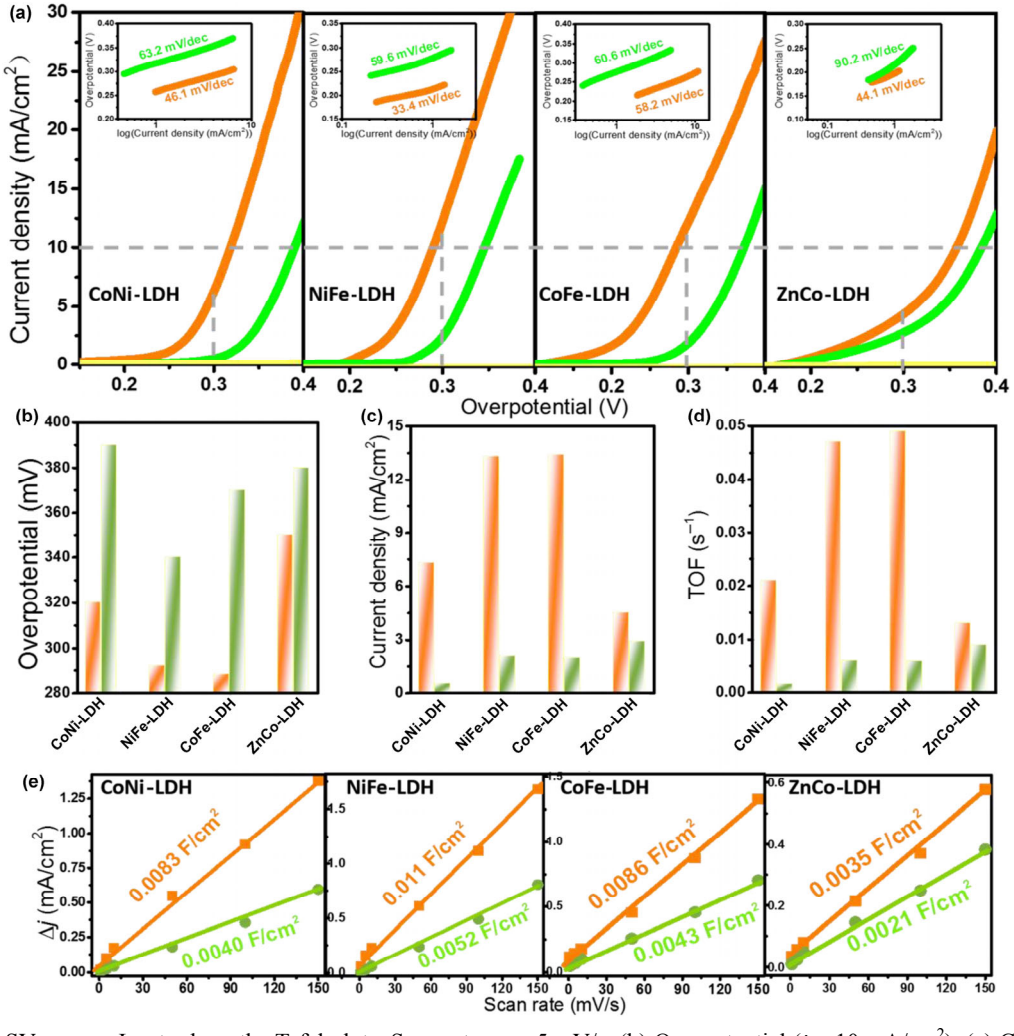

Figure 2 (a) LSV curves. Insets show the Tafel plots. Scan rate was 5 mV/s. (b) Overpotential (j = 10 mA/cm^2). (c) Current densities at η = 300 mV. (d) TOF calculated from current densities at η = 300 mV. (e) Charging current density differences plotted against scan rates. The linear slope is equivalent to twice the C_{dl}. The ultrathin single-unit-cell-thick LDH NSs: orange line; bulk LDHs: green line.

NiFe-, CoFe-, and ZnCo-LDHs were 63.2, 59.6, 70.6, and 90.2 mV/decade, respectively. The lower Tafel slopes for the single-unit-cell-thick LDH NSs suggest that electron transport is more efficient on the single-layer nanosheets than in the bulk LDHs.

TOF is also a key kinetic parameter for OER, indicating the intrinsic properties of electrocatalytic activity. Here, the TOF was estimated by assuming that all the electroactive metal atoms in the LDH NSs were catalytically active for the OER. The activity of the ultrathin single-unit-cell-thick LDH NSs is expressed in apparent TOF (Fig. 2(d)); thus, the ultrathin LDH NSs show better electrochemical OER performance than their bulk counterparts. In addition, C_{dl} (Fig. 2(e)) measurements were conducted to estimate the electrochemically active areas. The ultrathin single-unit-cell-thick LDH NSs showed much higher C_{dl} values than the bulk samples. The C_{dl} values of CoNi-, NiFe-, CoFe-, and ZnCo-LDH NSs were 4.15, 5.50, 4.30, and 1.74 mF/cm^2, whereas those of the bulk CoNi-, NiFe-, CoFe-, and ZnCo-LDHs were 2.0, 2.60, 2.15, and 1.05 mF/cm^2, respectively, revealing that the ultrathin single-unit-cell-thick LDH NSs have advantages in terms of enlarging the active surface area associated with more catalytically active sites.

The electrocatalytic activity of the NiFe-LDH NSs was the highest among the four ultrathin single-unit-cell-thick LDH NSs. Thus, the NiFe-LDH system was chosen to compare with IrO_2, a state-of-the-art high-efficiency OER catalyst. As shown in Fig. 3(a), the single-unit-cell-thick NiFe-LDH NSs outperformed the IrO_2 nanoparticles. The stability of the ultrathin single-unit-cell-thick LDH NSs was also tested at a high overpotential. Figure 3(b) shows that the ultrathin NiFe-LDH NSs had good electrochemical stability at high overpotential (370 mV) because the current density (30 mA/cm^2) remained nearly constant over 8 h. In contrast, the current density of the bulk NiFe-LDHs gradually decreased over an extended period at the same overpotential (370 mV). For IrO_2 nanoparticles (Fig. 3(b)), the current density had two significant reducing stages over 8 h, indicating the relatively

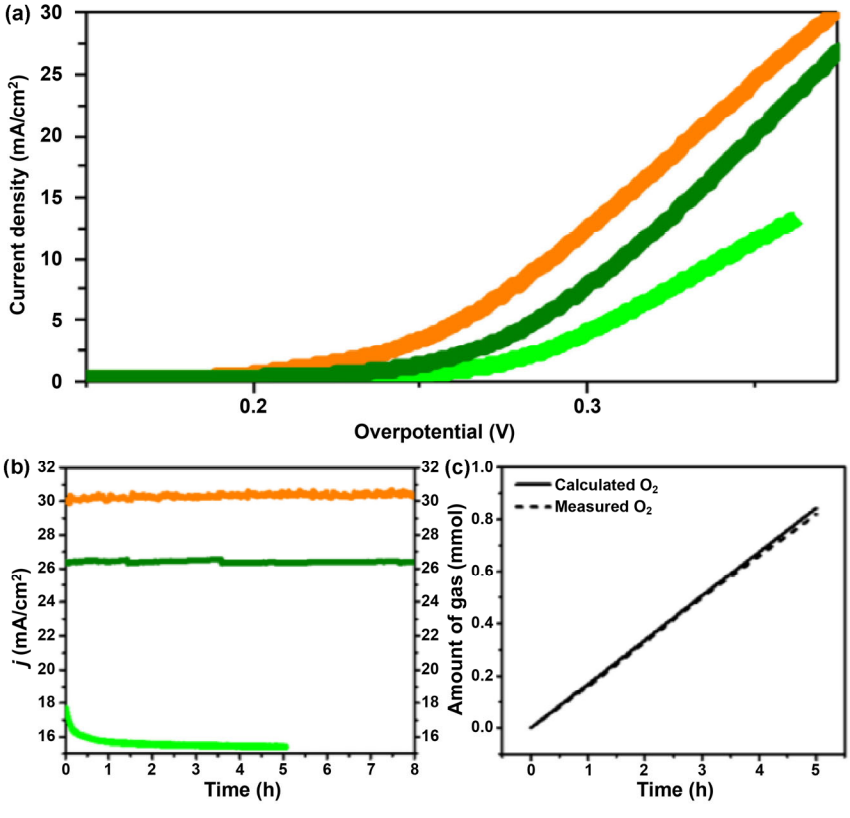

Figure 3 (a) LSV curves and (b) *I*–*t* curve at η = 370 mV vs. RHE for the ultrathin single-unit-cell NiFe-LDH NSs (orange line): bulk NiFe-LDHs (green line); IrO_2 nanoparticles (blue line). (c) The amount of gas (theoretically calculated and experimentally measured) vs. time for water splitting.

lower stability of IrO_2 as compared to the NiFe-LDH NSs. Moreover, after 8 h, the LSV curve of the NiFe-LDH NSs almost overlaps with its initial state, whereas the current density for IrO_2 and bulk NiFe-LDHs decreased at 370 mV (Fig. S10 in the ESM). The other three ultrathin LDH NSs also exhibited better stability than their bulk counterparts (Figs. S11 and S12 in the ESM). Moreover, the NiFe-LDH NSs showed nearly 100% faradaic efficiency for OER at high overpotential (370 mV, Fig. 3(c)).

To uncover the high ORE performance and to better understand the surface state and electron density information of the NiFe-LDH NSs, positron annihilation lifetime spectroscopy (PALS) was carried out [42, 44]. First, the positron annihilation lifetime is longer when the electronic density of a material is low. Second, as compared to idealized lattices, the electron density of defects is lower and electronegative. Typically, PALS is a non-destructive spectroscopy technique to study defects in solids. Herein, to reveal the surface defects of the NiFe-LDHs, positron annihilation lifetime values were obtained based on the positron lifetime components (τ_1, τ_2, and τ_3), as well as the relative intensities (I_1, I_2, and I_3, Fig. S13 in the ESM and Table 1). For the ultrathin single-unit-cell-thick NiFe-LDH NSs and bulk systems, the positron lifetime values were 0.35 and 0.31 ns, respectively, suggesting that the number of defects increased for the ultrathin NiFe-LDHs NSs. On the other hand, the possibility of positron trapping at defects sites is higher with the increasing of the concentration of defects. In this case, the relative intensity (I_3) of the positron long-lifetime component (τ_3) could reflect the concentration of defects. It is shown that the τ_3 values of the ultrathin single-unit-cell-thick NiFe-LDH NSs and the bulk NiFe-LDHs were the same (2.368 ns). However, the relative intensity of I_3 for the ultrathin NiFe-LDH NSs was much higher (2.654%) than that of the bulk system (1.899%) (Table 1). The higher relative intensity (I_3) of the positron long-lifetime τ_3 shows that the ultrathin single-unit-cell-thick NiFe-LDH NSs had a higher defect concentration and higher active site density than the bulk LDHs because defects can usually serve as active sites for OER [43, 45, 46].

Table 1 The positron annihilation lifetime data of the ultrathin single-unit-cell-thick NiFe-LDH NSs and the bulk system

Sample	τ_1 (ns)	I_1 (%)	τ_2 (ns)	I_2 (%)	τ_3 (ns)	I_3 (%)
Single-unit-cell thick NiFe-LDHs	0.1831	31.0	0.3465	66.3	2.368	2.654
Bulk NiFe-LDHs	0.1750	40.3	0.3346	57.9	2.368	1.899

Although LDHs have been used as OER catalysts, fundamental knowledge on their detailed energy structures is still limited. In this work, to gain insight into the electronic state information of the LDH NSs, periodic density functional theoretical (PDFT) calculations were performed on ideal models of CoFe-, CoNi-, NiFe-, and ZnCo-LDHs. The total and partial electronic densities of state (TDOS and PDOS, respectively, Fig. 4 and Figs. S14–S17 in the ESM) showed that the four typical LDH systems have small band gaps, with values of 0.194, 0.107, 0.410, and 0.878 eV, respectively (Fig. S18 in the ESM). It is obvious that the lower OER performance of the ZnCo-LDHs could correspond to the weak electron conductivity and the relative large band gap. Additionally, the top of the valence band (TVB) and the bottom of the conducting band (BCB) of the ZnCo-LDHs are mainly dominated by the d atomic orbitals of Co, suggesting the lack of obvious electronic transfer between the $Co(OH)_2$ and $Zn(OH)_2$ units. However, for CoFe-LDHs and NiFe-LDHs, the TVB and BCB are populated on both metal cluster units, and the PDOS profiles of majority spin and minority spin on metals (such as Fe elements in CoFe-LDHs and NiFe-LDHs) present an unsymmetrical distribution. Recently, Fe-based OER catalysts have attracted great interest. The excellent OER performance of Fe-based catalysts derives from the intrinsic semiconductor/metal characteristics and unique electronic structures, which could improve the electrical conductivity and the adsorption of H_2O [47–50]. The observations in this work show that electron spin-polarization may also play an important role in the electronic transport, which is consistent with the fact that Fe-based LDHs present high electrocatalytic activity during OER reactions in experiments and other as-reported works [51–54].

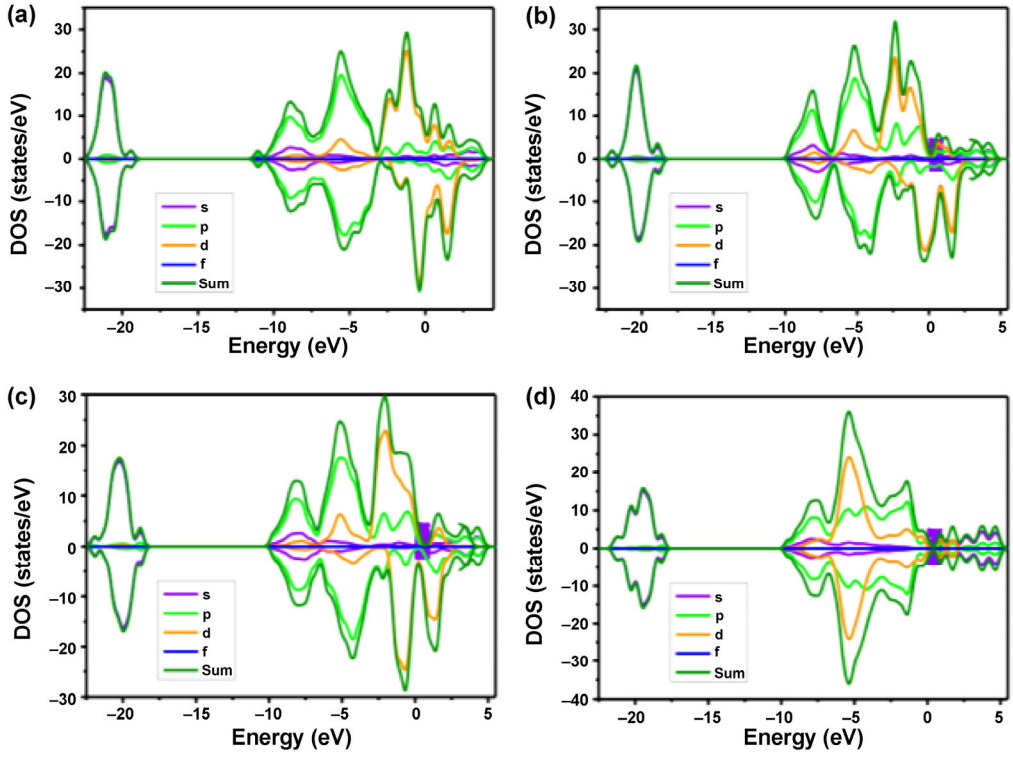

Figure 4 TDOS and PDOS calculated for the ultrathin single-unit-cell-thick systems for (a) CoFe-, (b) CoNi-, (c) NiFe-, and (d) ZnCo-LDHs.

4 Conclusions

In summary, 2D LDHs NSs were synthesized through a facile and rapid precipitation process. The resulting NSs showed single-unit-cell thickness and rich surface defect states. The as-prepared ultrathin single-unit-cell-thick LDH NSs exhibited highly active electrocatalysts for OER in water splitting, competing favorably against the bulk LDHs, as well as against a commercial state-of-the-art IrO_2 catalyst. The significantly higher catalytic activity of the ultrathin single-unit-cell-thick LDH NSs mainly originated from the increase in active site density and C_{dl} values. DFT calculations further provided a fundamental understanding of their electronic structures and spin-polarization, confirming the high electron conductivity of Co- and Fe-based LDHs for the OER process. It can be expected that, benefiting from the advantages of facile procedure and easy scale-up, this approach can be applicable and extended to the fabrication of other single-unit-cell-thick and defect-rich LDH systems for novel catalysts and renewable energy applications.

Acknowledgements

This work was supported by the National Basic Research Program of China (No. 2014CB932103), the National Natural Science Foundation of China (Nos. 21301016 and 21473013), and the Beijing Municipal Natural Science Foundation (No. 2152016).

Electronic Supplementary Material: Supplementary material (XRD patterns of colloid and the re-stacking ultrathin single-unit-cell-thick LDHs; AFM image and the corresponding height profiles, chemical compositions, TEM image and HRTEM image; the particle size distribution, and zeta potential of ultrathin single-unit-cell-thick LDH; XRD patterns and SEM images of bulk LDHs; XRD pattern, and SEM image of IrO_2; polarization curves before and after *I–t* curves; *I–t* curves versus RHE; polarization curves before and after *I–t* curves; the photograph and particle size distribution of NiFe-LDHs NSs dispersion in the 30 days; the positron annihilation lifetime spectra of NiFe-LDHs; TDOS and PDOS, and band structures)

is available in the online version of this article at https://doi.org/10.1007/s12274-017-1806-x.

References

[1] Turner, J. A. Sustainable hydrogen production. *Science* **2004**, *305*, 972–974.

[2] Rausch, B.; Symes, M. D.; Chisholm, G.; Cronin, L. Decoupled catalytic hydrogen evolution from a molecular metal oxide redox mediator in water splitting. *Science* **2014**, *345*, 1326–1330.

[3] Kanan, M. W.; Nocera, D. G. *In situ* formation of an oxygen-evolving catalyst in neutral water containing phosphate and Co^{2+}. *Science* **2008**, *321*, 1072–1075.

[4] Zhou, W. J.; Wu, X. J.; Cao, X. H.; Huang, X.; Tan, C. L.; Tian, J.; Liu, H.; Wang, J. Y.; Zhang, H. Ni_3S_2 nanorods/Ni foam composite electrode with low overpotential for electrocatalytic oxygen evolution. *Energy Environ. Sci.* **2013**, *6*, 2921–2924.

[5] Petrykin, V.; Macounova, K.; Shlyakhtin, O. A.; Krtil, P. Tailoring the selectivity for electrocatalytic oxygen evolution on ruthenium oxides by zinc substitution. *Angew. Chem., Int. Ed.* **2010**, *49*, 4813–4815.

[6] Grewe, T.; Deng, X. H.; Weidenthaler, C.; Schüth, F.; Tüysüz, H. Design of ordered mesoporous composite materials and their electrocatalytic activities for water oxidation. *Chem. Mater.* **2013**, *25*, 4926–4935.

[7] Zhang, J. T.; Zhao, Z H..; Xia, Z. H.; Dai, L. M. A metal-free bifunctional electrocatalyst for oxygen reduction and oxygen evolution reactions. *Nat. Nanotechnol.* **2015**, *10*, 444–452.

[8] Chen, S.; Duan, J. J.; Jaroniec, M.; Qiao, S. Z. Three-dimensional N-doped graphene hydrogel/NiCo double hydroxide electrocatalysts for highly efficient oxygen evolution. *Angew. Chem., Int. Ed.* **2013**, *52*, 13567–13570.

[9] Morales-Guio, C. G.; Stern, L. A.; Hu, X. L. Nanostructured hydrotreating catalysts for electrochemical hydrogen evolution. *Chem. Soc. Rev.* **2014**, *43*, 6555–6569.

[10] Louie, M. W.; Bell, A. T. An investigation of thin-film Ni–Fe oxide catalysts for the electrochemical evolution of oxygen. *J. Am. Chem. Soc.* **2013**, *135*, 12329–12337.

[11] Sun, Y. F.; Gao, S.; Lei, F. C.; Liu, J. W.; Liang, L.; Xie, Y. Atomically-thin non-layered cobalt oxide porous sheets for highly efficient oxygen-evolving electrocatalysts. *Chem. Sci.* **2014**, *5*, 3976–3982.

[12] Zheng, Y.; Jiao, Y.; Qiao, S. Z. Engineering of carbon-based electrocatalysts for emerging energy conversion: From fundamentality to functionality. *Adv. Mater.* **2015**, *27*, 5372–5378.

[13] Trotochaud, L.; Ranney, J. K.; Williams, K. N.; Boettcher, S. W. Solution-cast metal oxide thin film electrocatalysts for oxygen evolution. *J. Am. Chem. Soc.* **2012**, *134*, 17253–17261.

[14] Walter, M. G.; Warren, E. L.; McKone, J. R.; Boettcher, S. W.; Mi, Q. X.; Santori, E. A.; Lewis, N. S. Solar water splitting cells. *Chem. Rev.* **2010**, *110*, 6446–6473.

[15] Fekete, M.; Hocking, R. K.; Chang, S. L. Y.; Italiano, C.; Patti, A. F.; Arena, F.; Spiccia, L. Highly active screen-printed electrocatalysts for water oxidation based on β-manganese oxide. *Energy Environ. Sci.* **2013**, *6*, 2222–2232.

[16] Zhao, Y.; Nakamura, R.; Kamiya, K.; Nakanishi, S.; Hashimoto, K. Nitrogen-doped carbon nanomaterials as non-metal electrocatalysts for water oxidation. *Nat. Commun.* **2013**, *4*, 2390.

[17] Gao, R.; Zhang, H.; Yan, D. P. Iron diselenide nanoplatelets: Stable and efficient water-electrolysis catalysts. *Nano Energy* **2017**, *31*, 90–95.

[18] Gong, M.; Li, Y. G.; Wang, H. L.; Liang, Y. Y.; Wu, J. Z.; Zhou, J. G.; Wang, J.; Regier, T.; Wei, F.; Dai, H. J. An advanced Ni-Fe layered double hydroxide electrocatalyst for water oxidation. *J. Am. Chem. Soc.* **2013**, *135*, 8452–8455.

[19] Song, F.; Hu, X. L. Exfoliation of layered double hydroxides for enhanced oxygen evolution catalysis. *Nat. Commun.* **2014**, *5*, 4477.

[20] Wu, J.; Ren, Z. Y.; Du, S. C.; Kong, L. J.; Liu, B. W.; Xi, W.; Zhu, J. Q.; Fu, H. G. A highly active oxygen evolution electrocatalyst: Ultrathin CoNi double hydroxide/CoO nanosheets synthesized via interface-directed assembly. *Nano Res.* **2016**, *9*, 713–725.

[21] Liang, L.; Cheng, H.; Lei, F. C.; Han, J.; Gao, S.; Wang, C. M.; Sun, Y. F.; Qamar, S.; Wei, S. Q.; Xie, Y. Metallic single-unit-cell orthorhombic cobalt diselenide atomic layers: Robust water-electrolysis catalysts. *Angew. Chem., Int. Ed.* **2015**, *54*, 12004–12008.

[22] Tian, J. Q.; Liu, Q.; Asiri, A. M.; Alamry, K. A.; Sun, X. P. Ultrathin graphitic C_3N_4 nanosheets/graphene composites: Efficient organic electrocatalyst for oxygen evolution reaction. *Chemsuschem* **2014**, *7*, 2125–2130.

[23] Sun, Y. F.; Gao, S.; Xie, Y. Atomically-thick two-dimensional crystals: Electronic structure regulation and energy device construction. *Chem. Soc. Rev.* **2014**, *43*, 530–546.

[24] Sun, Y. F.; Gao, S.; Lei, F. C.; Xiao, C.; Xie, Y. Ultrathin two-dimensional inorganic materials: New opportunities for solid state nanochemistry. *Acc. Chem. Res.* **2015**, *48*, 3–12.

[25] Chen, S. C.; Kang, Z. X.; Hu, X.; Zhang, X. D.; Wang, H.; Xie, J. F.; Zheng, X. S.; Yan, W. S.; Pan, B. C.; Xie, Y. Delocalized spin states in 2D atomic layers realizing enhanced electrocatalytic oxygen evolution. *Adv. Mater.* **2017**, *29*, 1701687.

[26] Gong, M.; Dai, H. J. A mini review of NiFe-based materials as highly active oxygen evolution reaction electrocatalysts. *Nano Res.* **2015**, *8*, 23–39.

[27] Gao, R.; Yan, D. P.; Evans, D. G.; Duan, X. Layer-by-layer assembly of long-afterglow self-supporting thin films with dual-stimuli-responsive phosphorescence and antiforgery applications. *Nano Res.* **2017**, *10*, 3606–3617.

[28] Gomes, S. C.; Bouizi, Y.; Fornés, V.; García, H. Layered double hydroxides as highly efficient photocatalysts for visible light oxygen generation from water. *J. Am. Chem. Soc.* **2009**, *131*, 13833–13839.

[29] Fan, G. L.; Li, F.; Evans, D. G.; Duan, X. Catalytic applications of layered double hydroxides: Recent advances and perspectives. *Chem. Soc. Rev.* **2014**, *45*, 7040–7066.

[30] Zhao, Y. F.; Li, B.; Wang, Q.; Gao, W.; Wang, C. J.; Wei, M.; Evans, D. G.; Duan, X.; O'Hare, D. NiTi-layered double hydroxides nanosheets as efficient photocatalysts for oxygen evolution from water using visible light. *Chem. Sci.* **2014**, *5*, 951–958.

[31] Zhang, C.; Zhao, J. W.; Zhou, L.; Li, Z. H.; Shao, M. F.; Wei, M. Layer-by-layer assembly of exfoliated layered double hydroxide nanosheets for enhanced electrochemical oxidation of water. *J. Mater. Chem. A* **2016**, *4*, 11516–11523.

[32] Han, N.; Zhao, F. P.; Li, Y. G. Ultrathin nickel-iron layered double hydroxide nanosheets intercalated with molybdate anions for electrocatalytic water oxidation. *J. Mater. Chem. A* **2015**, *3*, 16348–16353.

[33] Yan, D. P.; Lu, J.; Wei, M.; Han, J. B.; Ma, J.; Li, F.; Evans, D. G.; Duan, X. Ordered poly(p-phenylene)/layered double hydroxide ultrathin films with blue luminescence by layer-by-layer assembly. *Angew. Chem., Int. Ed.* 2009, **48**, 3073–3076.

[34] Yan, D. P.; Lu, J.; Ma, J.; Wei, M.; Evans, D. G.; Duan, X. Reversibly thermochromic, fluorescent ultrathin films with a supramolecular architecture. *Angew. Chem., Int. Ed.* **2011**, *50*, 720–723.

[35] Yu, J. F.; Martin, B. R.; Clearfield, A.; Luo, Z. P.; Sun, L. Y. One-step direct synthesis of layered double hydroxide single-layer nanosheets. *Nanoscale* **2015**, *7*, 9448–9451.

[36] Gao, R.; Yan, D. P. Layered host–guest long-afterglow ultrathin nanosheets: High-efficiency phosphorescence energy transfer at 2D confined interface. *Chem. Sci.* **2017**, *8*, 590–599.

[37] Delley, B. From molecules to solids with the DMol3 approach. *J. Chem. Phys.* **2000**, *113*, 7756–7764.

[38] Dmol3 Module. *MS Modeling*, Version 2.2; Accelrys Inc.: San, Diego, CA, USA, 2003.

[39] Perdew, J. P.; Chevary, J. A.; Vosko, S. H.; Jackson, K. A.; Pederson, M. R.; Singh, D. J.; Fiolhais, C. Atoms, molecules, solids, and surfaces: Applications of the generalized gradient approximation for exchange and correlation. *Phys. Rev. B* **1992**, *46*, 6671–6687.

[40] Zhao, Y. B.; Hu, H.; Yang, X. X.; Yan, D. P.; Dai, Q. Tunable electronic transport properties of 2D layered double hydroxide crystalline microsheets with varied chemical compositions. *Small* **2016**, *12*, 4471–4476.

[41] Abellan, G.; Coronado, E.; Martí-Gastaldo, C.; Pinilla-Cienfuegos, E.; Ribera, A. Hexagonal nanosheets from the exfoliation of Ni^{2+}-Fe^{3+} LDHs: A route towards layered multifunctional materials. *J. Mater. Chem.* **2010**, *20*, 7451–7455.

[42] Liu, Z. P.; Ma, R. Z.; Osada, M.; Iyi, N.; Ebina, Y.; Takada, K.; Sasaki, T. Synthesis, anion exchange, and delamination of Co-Al layered double hydroxide: Assembly of the exfoliated nanosheet/polyanion composite films and magneto-optical studies. *J. Am. Chem. Soc.* **2006**, *128*, 4872–4880.

[43] Yan, D. F.; Li, Y. X.; Huo, J.; Chen, R.; Dai, L. M.; Wang, S. Y. Defect chemistry of nonprecious-metal electrocatalysts for oxygen reactions. *Adv. Mater.* **2017**, *29*, 1606459.

[44] Chen, H.; He, S.; Cao, X. Z.; Zhang, S. T.; Xu, M.; Pu, M.; Su, D. S.; Wei, M.; Evans, D. G.; Duan, X. Ru-cluster-modified Ni surface defects toward selective bond breaking between C–O and C–C. *Chem. Mater.* **2016**, *28*, 4751–4761.

[45] Liu, R.; Wang, Y. Y.; Liu, D. D.; Zou, Y. Q.; Wang, S. Y. Water-plasma-enabled exfoliation of ultrathin layered double hydroxide nanosheets with multivacancies for water oxidation. *Adv. Mater.* **2017**, *29*, 1701546.

[46] Wang, Y. Y.; Liu, D. D.; Liu, Z. J.; Xie, C.; Huo, J.; Wang, S. Y. Porous cobalt-iron nitride nanowires as excellent bifunctional electrocatalysts for overall water splitting. *Chem. Commun.* **2016**, *52*, 12614–12617.

[47] Indra, A.; Menezes, P. W.; Sahraie, N. R.; Bergmann, A.; Das, C.; Tallarida, M., Schmeisser, D.; Strasser, P.; Driess, M. Unification of catalytic water oxidation and oxygen reduction reactions: Amorphous beat crystalline cobalt iron oxides. *J. Am. Chem. Soc.* **2014**, *136*, 17530–17536.

[48] Jia, X. D.; Zhao, Y. F.; Chen, G. B.; Shang, L.; Shi, R.; Kang, X. F.; Waterhouse, G. I. N.; Wu, L. Z.; Tung, C. H.; Zhang, T. R. Ni_3FeN nanoparticles derived from ultrathin NiFe-layered double hydroxide nanosheets: An efficient overall water splitting electrocatalyst. *Adv. Energy Mater.* **2016**, *25*, 1502585.

[49] Fillol, J. L.; Codolà, Z.; Garcia-Bosch, I.; Gómez, L.; José Pla, J.; Costas, M. Efficient water oxidation catalysts based on readily available iron coordination complexes. *Nat. Chem.* **2011**, *3*, 807–813.

[50] Suntivich, J.; May, K. J.; Gasteiger, H. A.; Goodenough, J. B.; Shao-Horn, Y. A perovskite oxide optimized for oxygen evolution catalysis from molecular orbital principles. *Science* **2011**, *334*, 1383–1385.

[51] Xie, C.; Wang, Y. Y.; Hu, K.; Tao, L.; Huang, X. B.; Huo, J.; Wang, S. Y. *In situ* confined synthesis of molybdenum oxide decorated nickel-iron alloy nanosheets from MoO_4^{2-} intercalated layered double hydroxides for the oxygen evolution reaction. *J. Mater. Chem. A* **2017**, *5*, 87–91.

[52] Wang, Y. Y.; Zhang, Y. Q.; Liu, Z. J.; Xie, C.; Feng, S.; Liu, D. D.; Shao, M. F.; Wang, S. Y. Layered double hydroxide nanosheets with multiple vacancies obtained by dry exfoliation as highly efficient oxygen evolution electrocatalysts. *Angew. Chem., Int. Ed.* **2017**, *56*, 5867–5871.

[53] Yang, N.; Tang, C.; Wang, K. Y.; Du, G.; Asiri, A. M.; Sun, X. P. Iron-doped nickel disulfide nanoarray: A highly efficient and stable electrocatalyst for water splitting. *Nano Res.* **2016**, *9*, 3346–3354.

[54] Meng, F. L.; Zhong, H. X.; Yan, J. M.; Zhang, X. B. Iron-chelated hydrogel-derived bifunctional oxygen electrocatalyst for high-performance rechargeable Zn-air batteries. *Nano Res.* **2017**, *10*, 4436–4447.